

Date of publication xxxx 00, 0000, date of current version xxxx 00, 0000.

Digital Object Identifier 10.1109/ACCESS.2017. Doi Number

# Unscrambling for Subgap Density-of-States in Multilayered MoS<sub>2</sub> Field Effect Transistors under DC Bias Stress via Optical Charge-Pumping Capacitance-Voltage Spectroscopy

Ga Won Yang<sup>a†</sup>, Seung Gi Seo<sup>b‡</sup>, Sungju Choi<sup>a†</sup>, Dae Hwan Kim<sup>a†</sup>, and Sung Hun Jin<sup>b†</sup>

<sup>a</sup>The School of Electrical Engineering, Kookmin University, Seoul 02703, South Korea

<sup>b</sup>Department of Electronic Engineering, Incheon National University, Incheon 22012, South Korea

<sup>‡</sup> G. W. Yang, S. G. Seo, and S. Choi contribute equally to this work.

<sup>†</sup> corresponding authors.

<sup>a</sup>E-mail: drlife@kookmin.ac.kr

<sup>b</sup>E-mail: shjin@inu.ac.kr

This work was partly supported by the Priority Research Centers Program through the National Research Foundation of Korea (NRF) funded by the Ministry of Education (NRF-2020R1A6A1A03041954) and in part by the National Research Foundation (NRF) funded by the Korean Ministry of Science and ICT under Grant 2016R1A5A1012966 and 2020R1A2B5B01001979.

**ABSTRACT** Herein, we quantitatively analyze the evolution of the subgap density of states (DOSs) for multilayered molybdenum disulfide (m-MoS<sub>2</sub>) field effect transistors (FETs) with bilayered SiN<sub>x</sub>/SiO<sub>x</sub> gate dielectrics under positive bias stress (PBS) and negative bias stress (NBS) by using optical charge-pumping capacitance-voltage spectroscopy. To decouple external gas ambient effects on device instability, hydrophobic fluoropolymers (cyclized transparent optical polymer; CYTOP) are employed for m-MoS<sub>2</sub> FETs followed by the evaluation of subgap-DOSs in the devices for the respective PBS (or NBS). Through extraction of subgap-DOSs and their deconvolution with an analytical model of acceptor (or donor)-like states, it is shown that the device instability is closely correlated with state transitions of DOSs, corresponding to shallow (or midgap) levels for monosulfur vacancy (V<sub>S</sub>) (or disulfur vacancy (V<sub>S2</sub>)). Moreover, after PBS, the initial states of V<sub>S</sub> (0) (or H<sub>S2</sub> (0)) transit toward V<sub>S</sub> (-1) (or H<sub>S2</sub> (-1)) via electron trapping, whereas the transition toward V<sub>S</sub> (0) and H<sub>S2</sub> (+1) during NBS is assessed from the initial V<sub>S</sub> (-1) and H<sub>S2</sub> (0) states. Furthermore, technology computer-aided design (TCAD) simulation based on the extracted DOSs properly replicates the measured I-V characteristics of m-MoS<sub>2</sub> FETs with (and without) CYTOP encapsulation. In this study, subgap-DOS characterization via optical charge pumping and validation of the quantitative evolution of subgap-DOSs suggest that this platform can be potentially beneficial for an in-depth understanding of the origins of device instability for transition metal dichalcogenide (MX<sub>2</sub>)-based FETs, where M is a transition metal and X is a chalcogenide.

**INDEX TERMS** MoS<sub>2</sub>, field effect transistor, density of state (DOS), bias stress instability, TCAD simulation

## I. INTRODUCTION

For the ultimate scaling of Si devices below sub 3 nm, direct tunneling leakage through the channel from the source to drain electrode can be problematic, leading to a large increase in standby power consumption [1-2]. Thus, transition metal dichalcogenides (TMDCs) with a sizable energy bandgap beyond graphene have attracted much attention as promising candidates for next-generation semiconductors. This is attributed to versatile properties, such as astonishing

electrostatic gate coupling and a high effective mass of electrons, leading to less direct tunneling leakage, no dangling bonds, and genuine optical/chemical properties [3-6]. With regard to the development of next-generation semiconductors, device instability is a mandatory issue to be resolved for practical applications at the circuit and system levels, and therefore, understanding the origins of device instability should be a priority [7-8]. Moreover, the reliability issue for next-generation semiconductors is a key challenge because

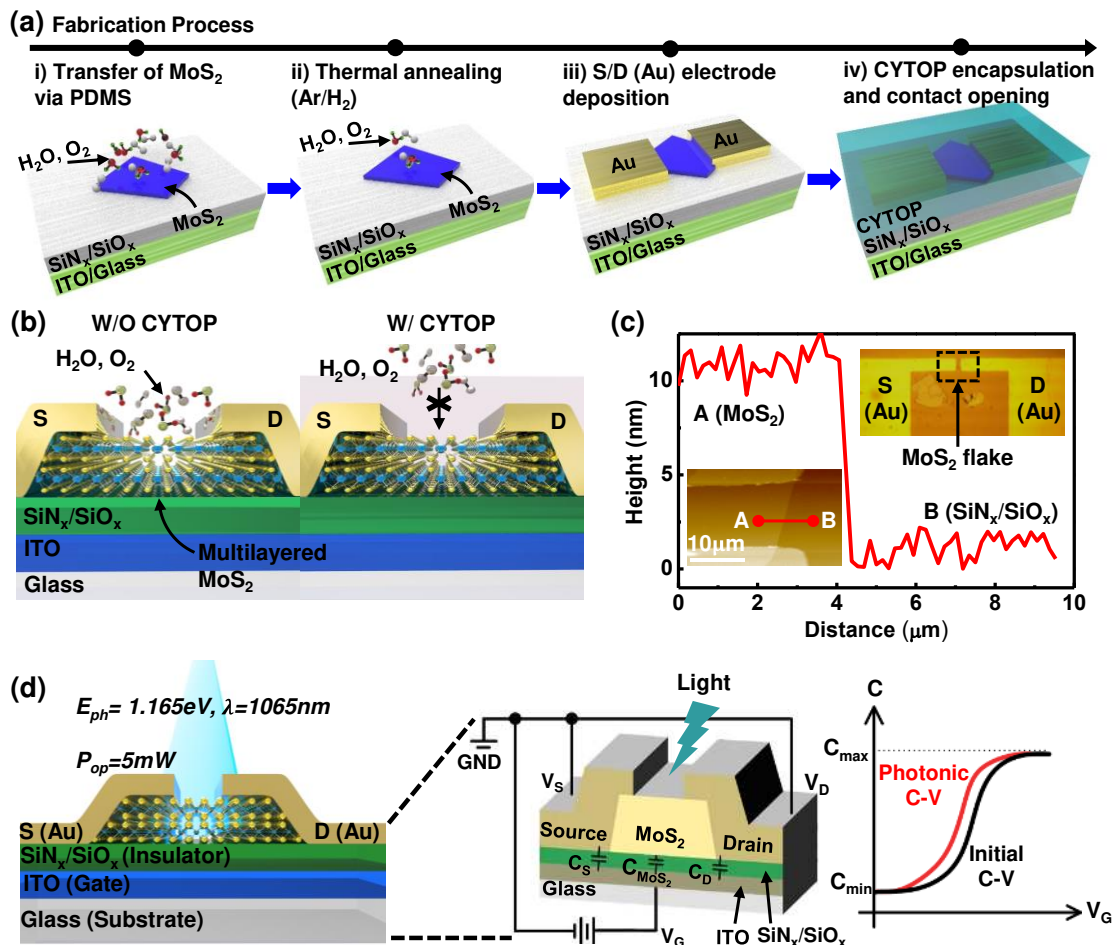


**FIG. 1.** (a) Fabrication process of m-MoS<sub>2</sub> FET with CYTOP passivation. (b) The whole device structures with and without CYTOP passivation. (c) Height profile for an m-MoS<sub>2</sub> flake in the channel regime scanned by AFM. Insets show optical microscope images for m-MoS<sub>2</sub> FETs. A and B in the inset denote the location of m-MoS<sub>2</sub> and oxide (SiO<sub>2</sub>), respectively. The channel width to length (W/L) is 30/10 μm (d) Conceptual plots for capacitance-voltage measurement captured by optical charge pumping technique.

newly explored materials are not mature enough; therefore, there is much room for improvement in material properties, process compatibility with Si technology, and wafer-scaled scalability, extending toward device- and circuit-level operation. Amongst the varieties of TMDCs, multilayered molybdenum disulfide (m-MoS<sub>2</sub>) is a suitable representative TMDC due to its easy exfoliation, relatively stable electrical properties, facile preparation, and abundant form of MoS<sub>2</sub> as natural minerals [9-10], leading to tremendous research activities that encompass various studies: basic transport mechanisms, device and circuit level demonstration toward FinFETs and flat panel displays, gas sensors, and emerging new concept of devices [11-20]. In the recent past, device performance improvement, understanding of genuine transport mechanisms in MoS<sub>2</sub> layers, and their electrical properties have been highly elucidated, and hence, an in-depth knowledge has automatically accumulated [20-23]. However, the improvement in understanding device reliability issues and their clear identification via novel electrical characterization methods are not fully quenched, albeit actively researched in the field of device physics [24-27]. In this sense, identification

of the subgap density of states (subgap-DOSs) in TMDCs and their correlation between operating conditions and device reliability are indispensable to the improvement of electrical parameters as well as device reliability in MoS<sub>2</sub> field effect transistors (FETs), which is a prerequisite for reliable operation in real applications. Thus, there have been significant activities to investigate the initial state of material properties via ab initio calculations and density of state characterization via optical charge pumping, Terman methods, and multifrequency C-V characterization [28-30]. However, there have been limited reports on detailed subgap-DOSs and their evolution for the corresponding bias stress for MoS<sub>2</sub> FETs, and moreover, the origin of subgap-DOSs and their variation associated with both external gas ambients (e.g., O<sub>2</sub>, H) and internal atomic structure deformation remain elusive even after tremendous research activity in this field [28-37]. This is possibly due to several hurdles: (i) the inability to prepare almost identical device ensembles associated with the absence of a mature, scalable process scheme for the preparation of active layers, (e.g., MoS<sub>2</sub> layers) with both high crystallinity and wafer-scaled substrates, (ii) limited scanning

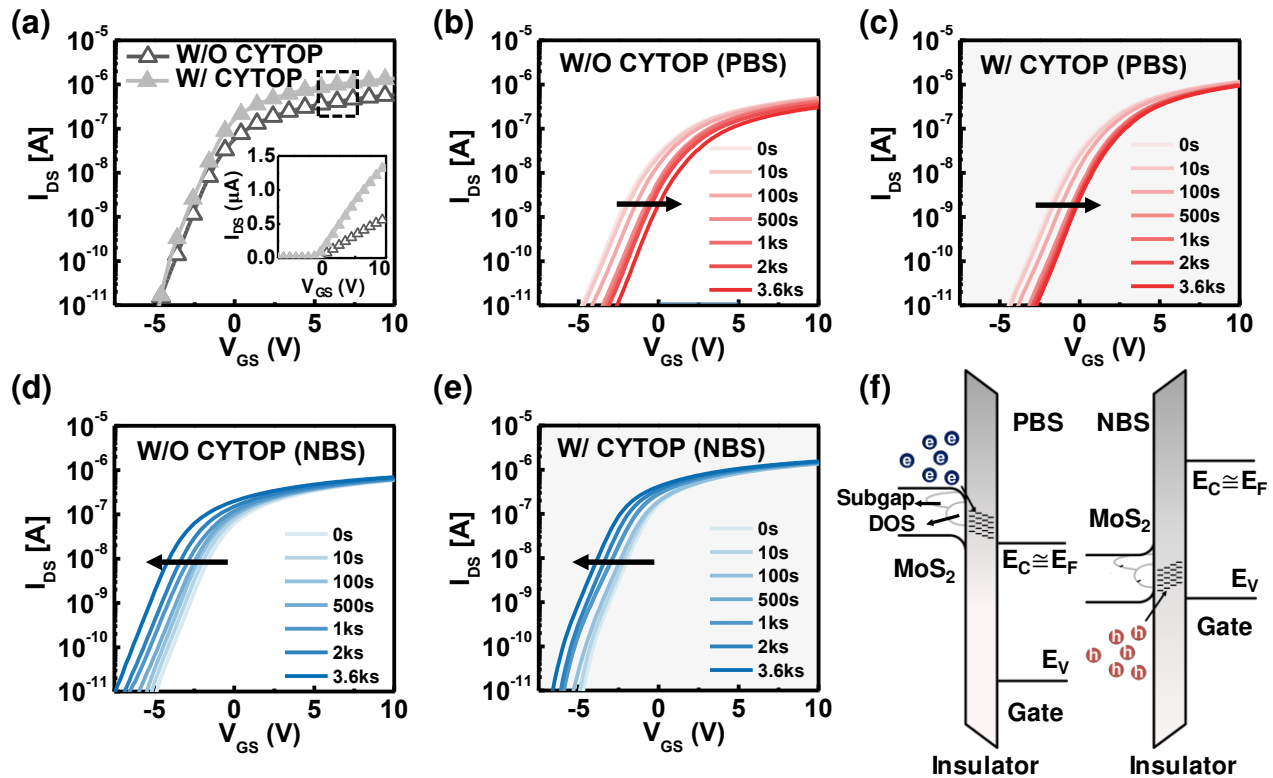


**FIG. 2.** (a) Comparison on initial transfer characteristics of m-MoS<sub>2</sub> FET without and with CYTOP encapsulation at  $V_{DS}=0.1$  V in log scale. Inset in Fig. 2(a) shows initial transfer characteristics of m-MoS<sub>2</sub> FET without and with CYTOP encapsulation at  $V_{DS}=0.1$  V in linear scale. (b) Transfer characteristics of m-MoS<sub>2</sub> FET without CYTOP encapsulation after PBS at  $V_{DS}=0.1$  V in log scale. (c) Transfer characteristics of m-MoS<sub>2</sub> FET with CYTOP encapsulation after PBS at  $V_{DS}=0.1$  V in log scale. (d) Transfer characteristics of m-MoS<sub>2</sub> FET without CYTOP encapsulation after NBS and (e) transfer characteristics of m-MoS<sub>2</sub> FET with CYTOP encapsulation after NBS at  $V_{DS}=0.1$  V in log scale. (f) Energy band diagrams to describe the charge trapping mechanisms of the m-MoS<sub>2</sub> FETs under PBS and NBS.

range for trap characterization based on conventional trap characterization methods such as Terman methods for  $D_{it}$  [29], multifrequency method for near conduction bands [30], and hysteretic gate transfer characteristics for deep level traps [31]. Thus, full-range characterization for subgap-DOSs is typically prohibited by the method itself and its characterization, leading to limited reports. However, there was a systematic report to characterize the full range of subgap-DOSs for m-MoS<sub>2</sub> FETs by using the optical charge pumping method, which has been popularly utilized and studied for the investigation of the reliability of a-IGZO TFTs with full maturity up to the commercialization level in AMOLED panels [38-43]. Interestingly, entire investigations on device reliability and its evolution on subgap-DOSs, corresponding to positive (or negative) bias stress (PBS or NBS), are completely missing, albeit specifically reported for initial subgap-DOSs for m-MoS<sub>2</sub> FETs with (or without) hydrophobic polymer (e.g., CYTOP) encapsulation [28].

On the other hand, there have been systematic reports on device instability on m-MoS<sub>2</sub> FETs under DC and pulsed mode operation, corresponding to positive and negative bias temperature stresses. Although in-depth studies on device instability for m-MoS<sub>2</sub> FETs were recently reported in the literature [44-45], thermal oxides (SiO<sub>2</sub>) on heavily phosphorus-doped Si substrates were used as gate dielectrics

for all devices, and therefore, device instability studies on m-MoS<sub>2</sub> FETs with one of the most popular gate dielectrics, for example, PECVD-based dielectrics, SiO<sub>x</sub> (or SiN<sub>x</sub>) in flat panel display backplanes, have not been explored. Furthermore, all analyses in previous reports have not addressed quantitative trap levels and their trap location in the energy bandgap of m-MoS<sub>2</sub> FETs for the corresponding positive or negative bias stress. Thus, the origin of device instability and quantitative evolution of subgap-DOSs according to the bias stress polarity and its time duration have not been explored for m-MoS<sub>2</sub> FETs with PECVD oxide gate dielectrics.

In the present work, we have investigated quantitative device instability for m-MoS<sub>2</sub> FETs by monitoring the evolution of subgap-DOSs via optical charge pumping, which was reliably well established in a systematic way in terms of quantitative analysis and TCAD-based validation. With a comparison of subgap-DOSs for positive and negative stress for m-MoS<sub>2</sub> FETs either with CYTOP encapsulation or without encapsulation, the contribution toward device instability associated with oxygen or moisture ( $\sim\text{OH}^-$ ) and subgap-DOSs are quantitatively analyzed. All origins and their device instability issues associated with subgap-DOSs, identified via the optical charge pumping method, are qualitatively analyzed, and their evolution for each trap and

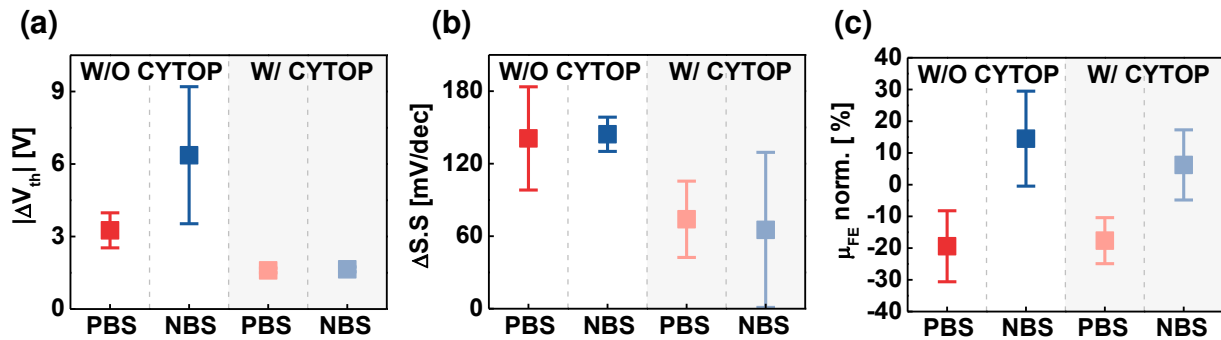


FIG. 3. (a)  $\Delta V_{th}$  in m-MoS<sub>2</sub> FET without and with CYTOP encapsulation after PBS and NBS. (b)  $\Delta S.S$  in m-MoS<sub>2</sub> FET without and with CYTOP encapsulation after PBS and NBS. (c) Normalized mobility in m-MoS<sub>2</sub> FET without and with CYTOP encapsulation after PBS and NBS.

device instability corresponding to subgap-DOSs are thoroughly interpreted in a quantitative mode, in comparison with conventionally accepted origins of device traps to address: (i) the effects of conduction band edge, Mo 4d orbital, (ii) valence band edge via hybridization of Mo 4d orbital and S 3 orbitals, and (iii) midgap states associated with disulfur vacancy, and (iv) shallow trap states correlated with monosulfur vacancy [46-48]. The entire analysis can provide us with insight into the physical origins behind the critical mechanisms that cause device instability behaviors for the respective PBS and NBS observed in this work, among the aforementioned candidates. Moreover, the origins of subgap-DOSs and their correlation between subgap-DOSs and O<sub>2</sub>, OH<sup>-</sup>, and sulfur vacancies are quantitatively analyzed and discussed. In addition, this study potentially suggests guidelines on how to improve device instability during operation and device implementation with a full understanding of the experimental results and their origins.

## II. EXPERIMENTAL METHOD

### A. Field effect transistor fabrication and characterization

Fig. 1(a) shows the process sequence for the fabrication of m-MoS<sub>2</sub> FETs. Indium tin oxide (ITO)-coated glass was used as a starting substrate, playing the role of a gate electrode, followed by ITO etching by dipping in ITO etchant solution to make an island structure. After etching, a gate insulator layer of SiN<sub>x</sub>/SiO<sub>2</sub> (200 nm/50 nm) was deposited by plasma-enhanced chemical vapor deposition (PECVD) at the substrate temperature of 350 °C without vacuum breaking, followed by a gate contact opening. Thereafter, multilayers of MoS<sub>2</sub> were mechanically exfoliated from bulk MoS<sub>2</sub> crystals (SPI Supplies, 429 ML-AB) and transferred onto ITO glass substrates using a polydimethylsiloxane (PDMS) elastomer. Immediate annealing was performed in a mixed gas (~Ar/H<sub>2</sub>) at 400 °C for 1 hour to remove organic residues from the MoS<sub>2</sub> flakes, which might contaminate them during the transfer process. Thereafter, a 30 nm thick layer of Au was evaporated using thermal evaporators, followed by lifting off on a photolithographically patterned area, forming the source/drain electrodes. The backside of the m-MoS<sub>2</sub> FETs was passivated

by amorphous fluorinated polymer (CYTOP; CTL-809 M, Asahi Glass Co., Ltd) using a spin coating process, followed by baking at 150 °C for 1 hour in a glove box with ambient Ar. Thereafter, dry etching (~O<sub>2</sub>/CF<sub>4</sub>) was performed to make open S/D contact pads for electrical addressing. The front view of the fabricated device is displayed in Fig. 1(b). Thereafter, atomic force microscopy (AFM), as shown in Fig. 1(c), confirmed that the thickness of the m-MoS<sub>2</sub> was 10 nm, which is equivalently extracted as 15 layers of MoS<sub>2</sub>. All electrical characterizations were measured with a semiconductor parameter analyzer (Agilent 4284A) in ambient air at room temperature. Transfer characteristics were obtained at V<sub>DS</sub> = 0.1 V. The thickness of the MoS<sub>2</sub> flakes was measured by atomic force microscopy (AFM, Park system, XE-100).

### B. Optical charge-pumping capacitance-voltage spectroscopy

In this study, for the extraction of subgap-DOSs in m-MoS<sub>2</sub> FETs, we utilized well-established optical charge-pumping capacitance-voltage (C-V) spectroscopy [38-39, 49]. The technique, as shown in Fig. 1(d), basically uses monochromatic photonic capacitance-voltage (MPCV) characterization. The capacitance between the bottom gate and S/D electrodes for m-MoS<sub>2</sub> FETs was evaluated in the dark and under light illumination with a laser wavelength ( $\lambda$ ) of 1065 nm. C-V characteristics were measured by an HP4284A precision LCR meter at a frequency of 10 kHz under dark and light illumination with a wavelength of  $\lambda = 1065$  nm to extract the full range of trap information in subband gaps. For the identification of subgap-DOSs for multilayered MoS<sub>2</sub>, a laser source with a wavelength of 1065 nm, which has an energy of  $E_{ph} = 1.24/\lambda_0 = 1.165$  eV, was used. In the present work, a wavelength of 1065 nm was intentionally selected in consideration of the energy bandgap of m-MoS<sub>2</sub> layers because lasers with wavelengths shorter than 1065 nm have a higher chance of exciting electrons located in the valence band toward conduction via band-to-band generation, leading to overestimation of the density of trapped charges. Moreover, optical power was selected in this work at a condition of 5 mW after confirming the saturation behaviors on photoresponse, which is similar to the method reported in the literature [28]. As shown in Fig. 1(d) middle, the minimum capacitance (C<sub>min</sub>)

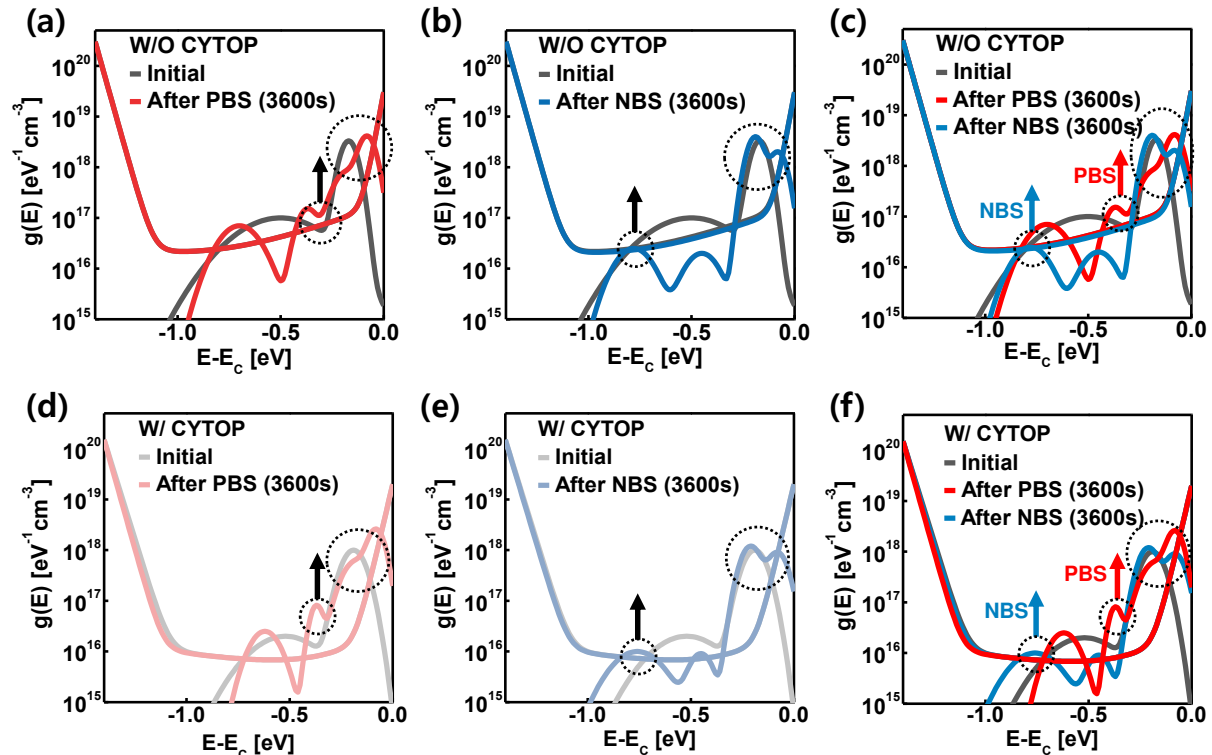


FIG. 4. Deconvoluted DOSs from the m-MoS<sub>2</sub> FET without CYTOP encapsulation (a) before and after PBS, (b) before and after NBS, and (c) overlapped data of Fig. 4(a) and (b). Deconvoluted DOSs from the m-MoS<sub>2</sub> FET with CYTOP encapsulation (d) before and after PBS, (e) before and after NBS, and (f) overlapped data of Fig. 4(d) and (e).

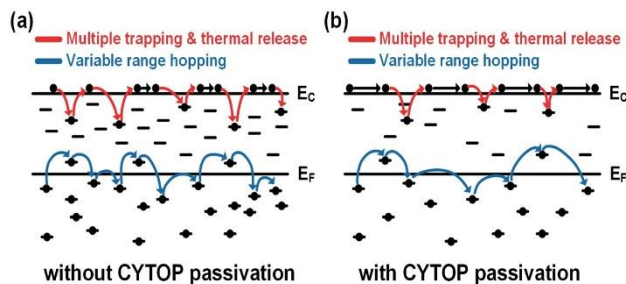


FIG. 5. Schematic cartoons to illustrate variable range hopping and multiple trapping and thermal release behaviors in m-MoS<sub>2</sub> FETs (a) with and (b) without CYTOP passivation

is determined by the total overlapping area between the source and drain electrodes ( $C_S$  and  $C_D$ ) and the gate electrodes. In addition, a conceptual capacitance-voltage plot, as shown in Fig. 1(d) on the right, shows that the capacitance difference ( $C_{\max} - C_{\min}$ ) between the maximum capacitance ( $C_{\max}$ ) and minimum capacitance ( $C_{\min}$ ) yields the capacitance for the active region of MoS<sub>2</sub> layers ( $C_{\text{MoS}_2}$ ), which can be modulated by gate-to-source voltage ( $V_{GS}$ ). These capacitance values can be differentiated before and after light illumination, yielding a difference in charge carriers in the MoS<sub>2</sub> channel due to optically pumped charge carriers from the inside bandgap of MoS<sub>2</sub> under light illumination. With this method, the photonic C-V and subgap-DOSs of m-MoS<sub>2</sub> FETs before and after bias stress can be measured, from which their correlation between subgap-DOSs and bias stress instability was investigated.

### C. TCAD validation

TCAD simulations were performed by incorporating the band structure, subgap density of the state model, advance mobility, and tunneling model into SILVACO ATLAS-2D. The band structure was simplified to several quantities: the energies of the conduction and valence band edges and the density-of-states masses for electrons and holes of each material. The trap-limited transport model was activated in this simulation. Additionally, an advanced mobility model including phonon scattering, Coulomb scattering, surface roughness, and subgap density of state effects was applied.

## III. RESULTS AND DISCUSSION

### A. Bias stress instability of m-MoS<sub>2</sub> FETs

For the evaluation of external gas ambient effects on the performance of m-MoS<sub>2</sub> FETs, CYTOP encapsulation was employed, and the initial electrical characteristics before encapsulation of CYTOP were evaluated with the same protocols reported in the literature [37]. For a fair comparative study, all electrical characteristics without and with CYTOP encapsulation were evaluated, and a systematic comparison was performed. Fig. 2(a) and its inset show transfer characteristics for m-MoS<sub>2</sub> FETs with and without CYTOP on a log scale and linear scale, respectively. Owing to outstanding encapsulation effects reported in the literature [37, 45, 50], suppression of external ambient gas effects (i.e., H<sub>2</sub>O and O<sub>2</sub>)

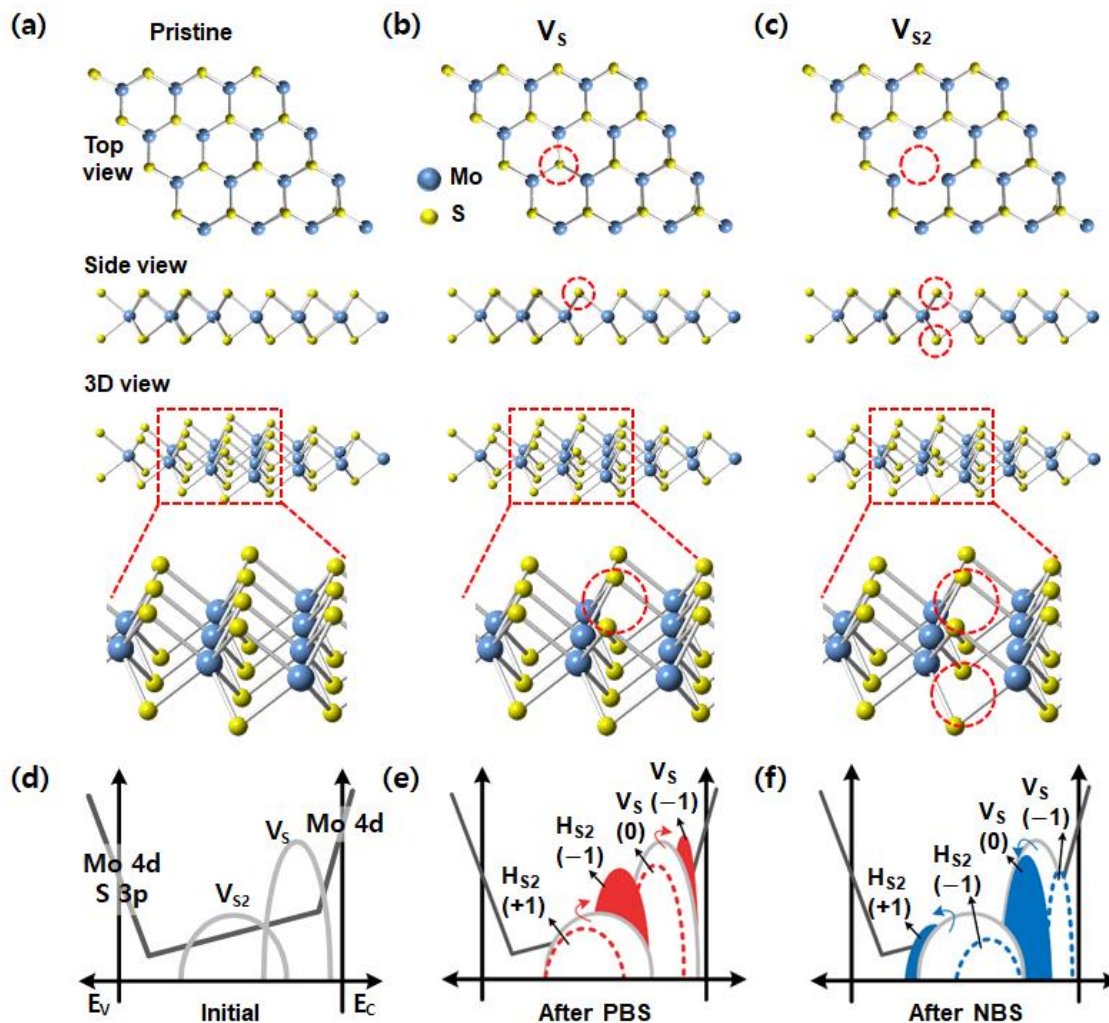


**FIG. 6.** Atomic structure for (a) pristine. (b) Monosulfur vacancy ( $V_S$ ). (c) Disulfur vacancy ( $V_{S2}$ ). Schematic cartoon about (d) initial DOSs model and DOSs model after (e) PBS and (f) NBS in m-MoS<sub>2</sub> FET.

on the back channel region of MoS<sub>2</sub> flakes leads to noticeable improvement of electrical properties on subthreshold swing (S.S) and field effect mobility ( $\mu_{FE}$ ). As external ambient gases were identified to cause additional trap sites in MoS<sub>2</sub> layers [34-37], encapsulation effects were shown to be closely related to instability issues. Figs. 2(b) and (c) show that a net threshold voltage shift ( $\Delta V_{th}$ ) is 2.3 V (or 1.9 V) for m-MoS<sub>2</sub> FETs without (or with) CYTOP under positive gate bias stress of 5 V, respectively, where  $V_{th}$  is extracted using constant current at  $I_{DS} = 10^{-8}$  A. Moreover, Figs. 2(d) and (e) show that the respective  $V_{th}$  shift is extracted as  $-2.6$  V (or  $-1.9$  V) for m-MoS<sub>2</sub> FETs without (or with) CYTOP encapsulation under a negative gate bias stress of  $-5$  V. The stress voltage was applied for approximately an hour considering the overdrive voltage. The reduced  $V_{th}$  shift value after CYTOP encapsulation substantiates the decrease in the total number of trap sites, which might originate from the back channel interface and defects inside the MoS<sub>2</sub> layers. Fig. 2(f) illustrates the bandgap models for charge trapping under bias stress conditions. Under PBS (or NBS), electrons (or holes)

can be trapped in both insulator and subgap-DOSs of m-MoS<sub>2</sub>. In particular, a larger  $V_{th}$  shift under negative bias stress for m-MoS<sub>2</sub> FETs with thermal gate oxide (SiO<sub>2</sub>) was frequently reported, which is attributed to the large population of hole traps, possibly coming from sulfur vacancies of MoS<sub>2</sub>, as observed in the previous literature [44-45]. However, the origin on different levels of  $\Delta V_{th}$  for the respective NBS (or PBS) may be attributed to the combination effects that result from gate dielectrics, their interface between an active layer and a gate dielectric, and the active layer itself. Hence, in this study, after CYTOP encapsulation, the absolute value of  $\Delta V_{th}$  for NBS is slightly larger than (or similar to) that of  $\Delta V_{th}$  for positive conditions, which is possibly due to synergetic effects coming from PECVD-based gate dielectrics and O<sub>2</sub> and H<sub>2</sub>O molecules.

With respect to the overall trend of electrical properties, Figs. 3(a), (b) and (c) show the detailed electrical properties, where S.S and  $\mu_{FE}$  are extracted from  $S.S = \{(\partial \log I_{DS} / \partial V_{GS})_{max}\}^{-1}$  and  $\mu_{FE} = L \cdot g_m (WC_i V_{DS})^{-1}$ . In addition to the reduction of  $\Delta V_{th}$ , the standard deviation for  $\Delta V_{th}$  and

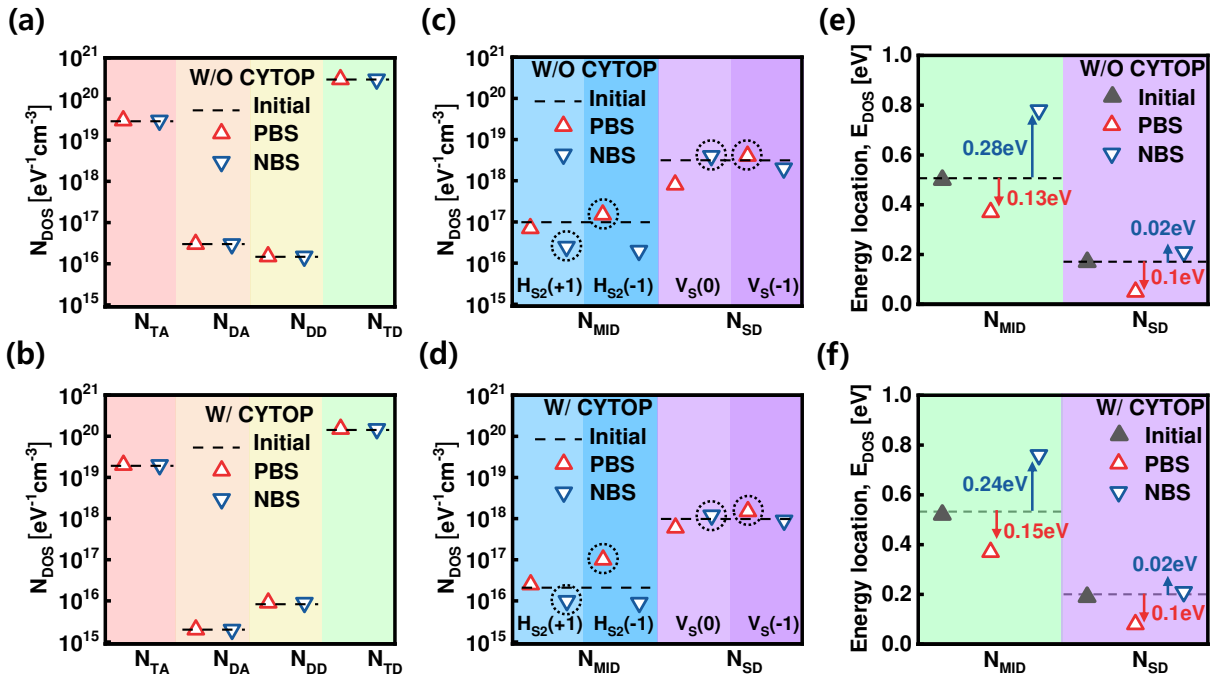


FIG. 7. Comparison on  $N_{TA}$ ,  $N_{DA}$ ,  $N_{DD}$ ,  $N_{TD}$ ,  $N_{MID}$ ,  $N_{SD}$  states level and their energy locations of m-MoS<sub>2</sub> FET (a), (c), (e) without and (b), (d), (f) with CYTOP encapsulation after PBS and NBS.

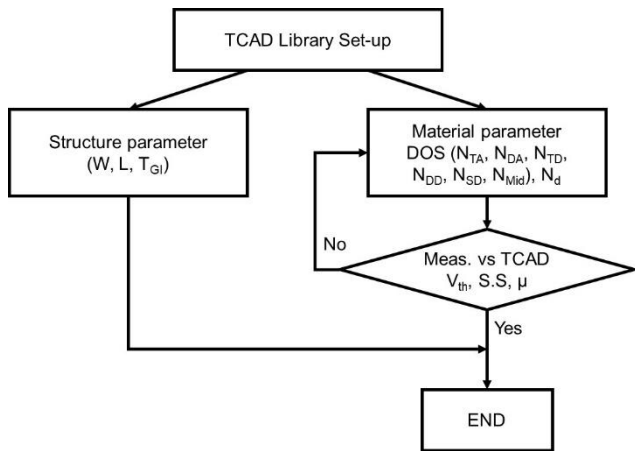


FIG. 8. Flow diagram for the TCAD simulation.

$\Delta\mu_{FE}$  is also remarkably reduced after CYTOP encapsulation, which enables us to secure uniform and improved stability properties of m-MoS<sub>2</sub> FETs regardless of device variation. On the other hand, bias stress effects on electrical properties, corresponding to a bias polarity during bias stress, were differently observed, according to the device encapsulation. Regardless of CYTOP encapsulation, the values of S.S increase for both PBS and NBS, whereas  $\mu_{FE}$  decreases (or increases) for PBS (or NBS). This behavior is possibly attributed to the change in trap densities and their distribution during device operation. However, if the apparently observed results stand alone, it could be highly uncertain to reach a reliable and detailed analysis on device instability because trap distribution and its variation are relatively hard to analyze by bias stress instability data and their instability model

standalone. In this regard, MPCV spectroscopy was adopted to investigate the fundamental origins of device instability, variation in electrical properties, and their correlation with subgap-DOSs of m-MoS<sub>2</sub>, which can evolve on a time scale during bias stress tests.

### B. Extraction of subgap-DOSs for m-MoS<sub>2</sub> FETs

Experimental platforms for optical charge pumping capacitance-voltage spectroscopy and their extraction procedures were reported in the literature [38-39]. Based on the measured photonic C-V characteristics and their standard procedures for the extraction of subgap-DOSs reported in the literature, subgap-DOSs for m-MoS<sub>2</sub> FETs, as shown in Fig. 4, were extracted and plotted, corresponding to positive (or negative) bias stress for m-MoS<sub>2</sub> FETs without (or with) CYTOP encapsulation. Acceptor-like states ( $g_A$ ) and donor-like states ( $g_D$ ), according to Equations (1) and (2), are analytically modeled and deconvoluted, yielding information on subgap-DOSs.

$$g_A(E) = g_{TA}(E) + g_{DA}(E) = N_{TA} \exp\left(-\frac{E_C - E}{kT_{TA}}\right) + N_{DA} \exp\left(-\frac{E_C - E}{kT_{DA}}\right) \quad (1)$$

$$g_D(E) = g_{TD}(E) + g_{DD}(E) + g_{SD}(E) + g_{Mid}(E) = N_{TD} \exp\left(-\frac{E - E_V}{kT_{TD}}\right) + N_{DD} \exp\left(-\frac{E - E_V}{kT_{DD}}\right) + N_{SD} \exp\left\{-\left(\frac{E_C - E_{SD} - E}{kT_{SD}}\right)^2\right\} + N_{Mid} \exp\left\{-\left(\frac{E - E_V - E_{Mid}}{kT_{Mid}}\right)^2\right\} \quad (2)$$

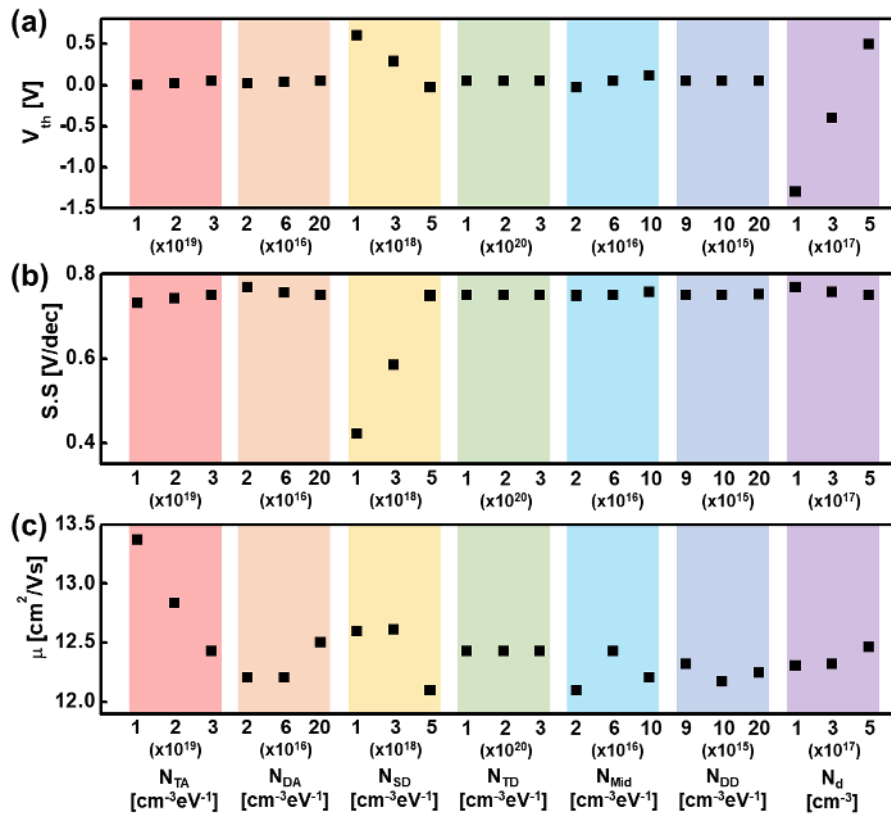


FIG. 9. Plots of electrical parameters such as (a)  $V_{th}$ , (b) S.S, and (c)  $\mu$ , corresponding to trap level variation,

, where  $g_{TA}(E)$  is for acceptor-like tail states,  $g_{DA}(E)$  for acceptor-like deep states,  $g_{TD}(E)$  for donor-like tail states,  $g_{DD}(E)$  for donor-like deep states,  $g_{SD}(E)$  for shallow-donor states, and  $g_{Mid}(E)$  for mid gap defect states, depending on the type of energy level distribution. In addition, the characteristic energy distribution and Gaussian center of energy are defined as  $kT_{DOS}$  (e.g.,  $T_{TA}$ ,  $T_{DA}$ ,  $T_{TD}$ ,  $T_{DD}$ ,  $T_{SD}$ , and  $T_{Mid}$ ) and  $E_{DOS}$  (e.g.,  $E_{SD}$ ,  $E_{Mid}$ ), respectively, and are extracted. Herein,  $N_{DOS}$  (e.g.,  $N_{TA}$ ,  $N_{DA}$ ,  $N_{TD}$ ,  $N_{DD}$ ,  $N_{SD}$ , and  $N_{Mid}$ ) represents each energy density distribution of traps,  $E_V$  represents the valance band maximum, and  $E_C$  represents the conduction band minimum, which are magnificently fitted with the model parameters represented by Equations (1) and (2). All extracted subgap-DOSs are fitted with the analytical models for Equations (1) and (2), leading to smooth functions for subgap-DOSs, as shown in Fig. 4. Subgap-DOSs are deconvoluted using conventional trap states such as acceptor-like states (e.g., Eq. (1)) and donor-like states (e.g., Eq. (2)), respectively, yielding information for a quantitative understanding. In particular, it is generally reported that the  $\mu_{FE}$  in n-channel FETs is significantly affected by defects near  $E_C$  [28]. Several key parameters, such as  $g_{TA}(E)$ ,  $g_{SD}(E)$ , and  $g_{DA}(E)$ , below  $E_C$  are energetically distributed throughout the energy bandgap with energy location dependency, yielding capture and thermal release of free carriers in certain energy states, such as multiple trapping and thermal release events [28]. Fig. 5 shows

schematic cartoons to illustrate the reduction of frequency in multiple trapping and release due to CYTOP passivation, which has the effects of prohibition of external gas adsorption toward sulfur vacancy, possibly located in defects in active layer of MoS<sub>2</sub> and interface between MoS<sub>2</sub> and gate dielectric. As per Fig. 5, the bias condition is the same condition corresponding to the same gate-overdrive voltage. In this sense, capture probability should be reduced when trap levels in forbidden bandgaps are reduced due to passivation. More importantly, field effect mobility improvement after passivation can be determined not by “trap level reduction itself” but by “how much reduction of trap levels”, which are located in the energy level around  $E_F$  at certain temperature and applied bias condition.

To better understand the characteristics of subgap-DOSs for m-MoS<sub>2</sub> FETs under bias stress, we extracted and analyzed detailed subgap-DOSs for m-MoS<sub>2</sub> FETs after the respective PBS (or NBS) for 1 hour. Fig. 4(a) (or (b)) shows deconvoluted curves for subgap-DOSs,  $g(E)$ , which are fitted with experimentally extracted DOSs for m-MoS<sub>2</sub> FETs without CYTOP encapsulation after positive (or negative) bias stress. For a better comparison, two data points are plotted in overlapping mode, which is displayed in Fig. 4(c). On the other hand, Fig. 4(d) (or (e)) shows deconvoluted curves for subgap-DOSs and  $g(E)$  for m-MoS<sub>2</sub> FETs with CYTOP encapsulation after positive (or negative) bias stress. For a



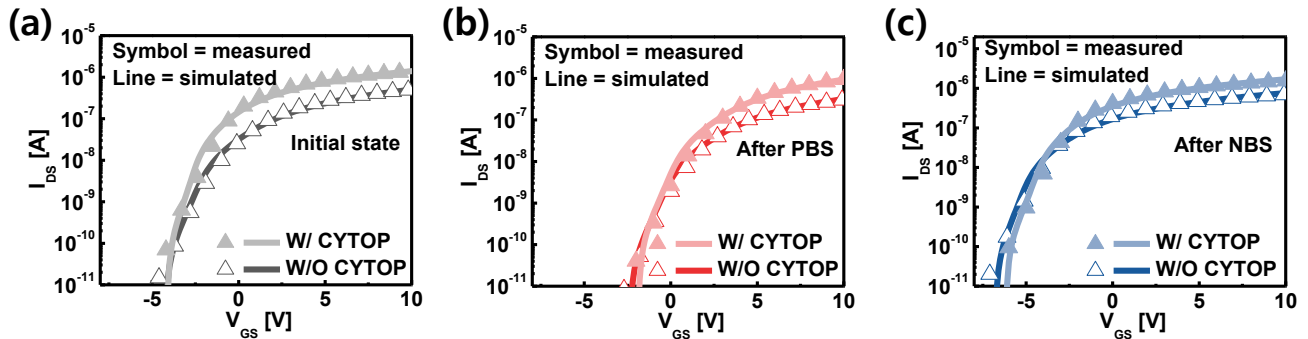


FIG. 10. Measured (Symbol) and T-CAD model-based (Line) (a) initial transfer characteristics and transfer characteristics after (b) PBS and (c) NBS in m-MoS<sub>2</sub> FET without and with CYTOP encapsulation.

clear and intuitive comparison, two data points overlap in the same graph, which is displayed in Fig. 4(f). After PBS for 1 hour, Fig. 4(a) (or (d)) illustrates that some values in the  $N_{SD}$  (or  $N_{Mid}$ ) peaks, which are located closer to  $E_C$  (or further away from  $E_V$ ), respectively, were increased for m-MoS<sub>2</sub> FETs regardless of CYTOP encapsulation. On the other hand, after NBS for 1 hour, Fig. 4(b) (or Fig. 4(e)) shows that some values in the  $N_{SD}$  (or  $N_{Mid}$ ) peaks, which are located further away from  $E_C$  (or closer to  $E_V$ ), increased for m-MoS<sub>2</sub> FETs regardless of CYTOP encapsulation. Overall, a noticeable change in DOSs was observed after PBS (or NBS), hinting that subgap states for m-MoS<sub>2</sub> were discernably changed, followed by redistribution of subgap states in the allowed DOSs. Thereafter, systematic modeling and extraction procedures are applied to subgap-DOS parameters, yielding quantitative values, as displayed in Fig. 4.

From the extracted and fitted DOS results, the atomic structure and DOSs model of MoS<sub>2</sub> are shown in Fig. 6. Figs. 6(a), (b), and (c) illustrate the atomic configuration in a MoS<sub>2</sub> layer for the respective views of top, side, and 3D, corresponding to a pristine monosulfur vacancy ( $V_S$ ) and a disulfur vacancy ( $V_{S_2}$ ) in m-MoS<sub>2</sub>. Fig. 6(d) indicates the DOSs model extracted from our m-MoS<sub>2</sub> FETs. As revealed in the literature [46-48, 51], the origin for each state could be conceived, accordingly, for the respective of (i) conduction band edge for Mo 4d orbital, (ii) valence band edge for hybridization of Mo 4d orbital and S 3p orbitals, (iii) midgaps for disulfur vacancy ( $V_{S_2}$ ), and (iv) possible shallow trap states for monosulfur vacancy ( $V_S$ ).

In the subgap DOSs of MoS<sub>2</sub>,  $V_S$  and  $V_{S_2}$  are dominant owing to their low formation energy [48]. However, other representative defects, such as molybdenum vacancies, were excluded owing to their very high formation energy [48, 52]. Figs. 6(e) and (f) indicate DOSs models after 1 hour of PBS and NBS, respectively [48, 52-54]. In particular, for the case of a disulfur vacancy, combination with hydrogen might occur, leading to transformation toward a hydrogenated disulfur vacancy ( $H_{S_2}$ ) [52]. During PBS, a shift of the Fermi energy level ( $E_F$ ) upwards results in the occupation of electrons onto the  $V_S$  state, which can be attributed to the transition toward  $V_S(-1)$  via the adoption of electrons, and moreover,  $H_{S_2}$  can

be changed into the  $H_{S_2}$  state (-1) due to the attraction of electrons. When the state transition for  $V_S$  and  $H_{S_2}$  predominantly occurred, the increase in states, according to the (-1) state peak of  $V_S$  and  $H_{S_2}$ , should be rationally expected. On the other hand, during NBS, the Fermi energy level ( $E_F$ ) moves downwards, and  $V_S(-1)$  can transition into the state of  $V_S(0)$  by combining with positive holes. In addition,  $H_{S_2}$  can be changed into the state of  $H_{S_2}(+1)$  by combining with positive holes. Thus, when a predominant transition can occur, the leading state change from  $V_S(-1)$  (or  $H_{S_2}$ ) to  $V_S(0)$  ( $H_{S_2}(+1)$ ), and the increase in peak states for  $V_S(0)$  (or  $H_{S_2}(+1)$ ) are rationally predicted after NBS stress.

For a quantitative comparison, detailed DOSs for all peaks and their energy location, corresponding to usage of encapsulation and bias stress condition, were compared in Fig. 7. Regardless of CYTOP encapsulation, Figs. 7(a), (b) show that the  $N_{TA}$ ,  $N_{DA}$ ,  $N_{DD}$ , and  $N_{TD}$  peaks remain in their original state even after PBS and NBS. However, compared to the information on DOSs for m-MoS<sub>2</sub> FETs without CYTOP, % reduction for the respective trap state after CYTOP encapsulation is estimated to be 33% for  $N_{TA}$ , 93% for  $N_{DA}$ , 50% for  $N_{TD}$ , and 40% for  $N_{DD}$ , which is consistent with the results of  $\Delta V_{th}$  reduction with CYTOP encapsulation in Fig. 3(a).

All results and their trends on the evolution for subgap-DOSs after CYTOP encapsulation are on the same page as previously reported data in the literature [28]. On the other hand, as mentioned before, Figs. 7(c) and (d) display that  $V_S(-1)$  (or  $H_{S_2}(-1)$ ) peaks after PBS were increased to the value of  $4 \times 10^{18}$  (or  $1.5 \times 10^{17}$ ) for the device without CYTOP and  $1.5 \times 10^{18}$  (or  $1 \times 10^{17}$ ) for the device with CYTOP, respectively, as compared to the value of  $8 \times 10^{17}$  (W/O CYTOP) and  $6 \times 10^{17}$  (W/CYTOP) for  $V_S(0)$  and the value of  $7 \times 10^{16}$  (W/O CYTOP) and  $2.5 \times 10^{16}$  (W/CYTOP) for  $H_{S_2}(+1)$ , accordingly. In addition,  $V_S(0)$  (or  $H_{S_2}(+1)$ ) peaks after NBS show higher values of  $4 \times 10^{18}$  (or  $2.5 \times 10^{16}$ ) for the device without CYTOP and  $1.2 \times 10^{18}$  (or  $1 \times 10^{16}$ ) for the device with CYTOP compared to the values of  $2 \times 10^{18}$  (W/O CYTOP) and  $9 \times 10^{17}$  (W/CYTOP) for  $V_S(-1)$  and  $2 \times 10^{16}$  (W/O CYTOP) and  $9 \times 10^{15}$  (W/CYTOP) for  $H_{S_2}(-1)$ , respectively.

**Table 1.** Summary of model parameters which are extracted from acceptor-like and donor-like states models to be fitted with subgap density of states ( $g(E)$ ) for m-MoS<sub>2</sub> FETs without CYTOP passivation after PBS (or NBS), respectively. Initial stands for m-MoS<sub>2</sub> FETs without PBS (or NBS).

DOSs W/O CYTOP		Initial	PBS	NBS
	$N_{TA} [eV^{-1}cm^{-3}] / kT_{TA} [eV]$	$3 \times 10^{19} / 0.02$	(identical for initial, PBS, NBS)	
	$N_{DA} [eV^{-1}cm^{-3}] / kT_{DA} [eV]$	$3 \times 10^{16} / 0.2$	(identical for initial, PBS, NBS)	
	$N_{DD} [eV^{-1}cm^{-3}] / kT_{DD} [eV]$	$1.5 \times 10^{16} / 0.85$	(identical for initial, PBS, NBS)	
	$N_{TD} [eV^{-1}cm^{-3}] / kT_{TD} [eV]$	$3 \times 10^{20} / 0.03$	(identical for initial, PBS, NBS)	
	$N_{Mid} [eV^{-1}cm^{-3}] / kT_{Mid} [eV] / E_{Mid} [eV]$	$1 \times 10^{17} / 0.25 / 0.5$	-	-
$N_{Mid}$	$N_{HS2(+)} [eV^{-1}cm^{-3}] / kT_{HS2(+)} [eV] / E_{HS2(+)} [eV]$	-	$7 \times 10^{16} / 0.12 / 0.7$	$2.5 \times 10^{16} / 0.11 / 0.78$
	$N_{HS2(-)} [eV^{-1}cm^{-3}] / kT_{HS2(-)} [eV] / E_{HS2(-)} [eV]$	-	$1.5 \times 10^{17} / 0.05 / 0.37$	$2 \times 10^{16} / 0.10 / 0.45$
	$N_{SD} [eV^{-1}cm^{-3}] / kT_{SD} [eV] / E_{SD} [eV]$	$3 \times 10^{18} / 0.06 / 0.17$	-	-
$N_{SD}$	$N_{VS(0)} [eV^{-1}cm^{-3}] / kT_{VS(0)} [eV] / E_{VS(0)} [eV]$	-	$8 \times 10^{17} / 0.08 / 0.18$	$4 \times 10^{18} / 0.05 / 0.19$
	$N_{VS(-)} [eV^{-1}cm^{-3}] / kT_{VS(-)} [eV] / E_{VS(-)} [eV]$	-	$4 \times 10^{18} / 0.08 / 0.05$	$2 \times 10^{18} / 0.05 / 0.08$

**Table 2.** Summary of model parameters which are extracted from acceptor-like and donor-like states models to be fitted with subgap density of states ( $g(E)$ ) for m-MoS<sub>2</sub> FETs with CYTOP passivation after PBS (or NBS), respectively. Initial stands for m-MoS<sub>2</sub> FETs without PBS (or NBS).

DOSs W/ CYTOP		Initial	PBS	NBS
	$N_{TA} [eV^{-1}cm^{-3}] / kT_{TA} [eV]$	$2 \times 10^{19} / 0.025$	(identical for initial, PBS, NBS)	
	$N_{DA} [eV^{-1}cm^{-3}] / kT_{DA} [eV]$	$2 \times 10^{15} / 0.2$	(identical for initial, PBS, NBS)	
	$N_{DD} [eV^{-1}cm^{-3}] / kT_{DD} [eV]$	$9 \times 10^{15} / 0.85$	(identical for initial, PBS, NBS)	
	$N_{TD} [eV^{-1}cm^{-3}] / kT_{TD} [eV]$	$1.5 \times 10^{20} / 0.03$	(identical for initial, PBS, NBS)	
	$N_{Mid} [eV^{-1}cm^{-3}] / kT_{Mid} [eV] / E_{Mid} [eV]$	$2 \times 10^{16} / 0.2 / 0.52$	-	-
$N_{Mid}$	$N_{HS2(+)} [eV^{-1}cm^{-3}] / kT_{HS2(+)} [eV] / E_{HS2(+)} [eV]$	-	$2.5 \times 10^{16} / 0.09 / 0.62$	$1 \times 10^{16} / 0.15 / 0.76$
	$N_{HS2(-)} [eV^{-1}cm^{-3}] / kT_{HS2(-)} [eV] / E_{HS2(-)} [eV]$	-	$1 \times 10^{17} / 0.04 / 0.37$	$9 \times 10^{15} / 0.07 / 0.45$
	$N_{SD} [eV^{-1}cm^{-3}] / kT_{SD} [eV] / E_{SD} [eV]$	$1 \times 10^{18} / 0.07 / 0.19$	-	-
$N_{SD}$	$N_{VS(0)} [eV^{-1}cm^{-3}] / kT_{VS(0)} [eV] / E_{VS(0)} [eV]$	-	$6 \times 10^{17} / 0.08 / 0.18$	$1.2 \times 10^{18} / 0.06 / 0.21$
	$N_{VS(-)} [eV^{-1}cm^{-3}] / kT_{VS(-)} [eV] / E_{VS(-)} [eV]$	-	$1.5 \times 10^{18} / 0.05 / 0.08$	$9 \times 10^{17} / 0.06 / 0.08$

For further confirmation of the peak transition of  $V_S$  and  $V_{S2}$  after bias stress, the energy location of each peak was extracted. Fig. 7(e) shows that the  $N_{Mid}$  peak with the highest value for the bare device W/O CYTOP was changed from the initial value of 0.50 eV to 0.37 eV (or 0.78 eV) after PBS (or NBS). On the other hand, the  $N_{SD}$  peak with the highest value for the bare device was changed from the initial value of 0.17 eV to 0.05 eV (or 0.19 eV) after PBS (or NBS), accordingly. Due to the transition of  $V_S$  and  $V_{S2}$  toward a negative state after PBS (or a positive state after NBS), the energy locations of the  $N_{Mid}$  and  $N_{SD}$  peaks, which are closely associated with  $V_S$  and  $V_{S2}$ , are shifted to near  $E_C$  (or toward  $E_V$ ). Likewise, for the W/CYTOP device, Fig. 7(f) shows that the  $N_{Mid}$  peak with the highest value was changed from the initial value of 0.52 eV to 0.37 eV (or 0.76 eV) after PBS (or NBS). Moreover, the  $N_{SD}$  peak with the highest value moved from the initial value of 0.19 eV to 0.08 eV (or 0.21 eV) after PBS (or NBS), respectively.

All results, as shown in Fig. 7, substantiate that the effects of bias stress for m-MoS<sub>2</sub> FETs are closely correlated with subgap states and that their information on the evolution of DOSs is beneficial to understand the quantitative contribution toward electrical parameters, including  $V_{th}$  and S.S, and  $\mu_{FE}$ , and others. Furthermore, these results are reasonably matched with the variation in electrical properties for m-MoS<sub>2</sub> FETs after bias stress. Similar to the evolution of electrical parameters in Fig. 3, S.S increases and  $\mu_{FE}$  decreases after PBS, and S.S and  $\mu_{FE}$  increase after NBS, respectively. The degradation on S.S after PBS (or NBS) might be attributed to the widened  $N_{SD}$  peak after bias stress. Moreover, the decreased  $\mu_{FE}$  after PBS can originate from an increase in impurity scattering, possibly due to the generation of  $V_S(-1)$  states during PBS. On the other hand, the variation in the evolution of  $\mu_{FE}$  according to the stress time of NBS was relatively small compared to that of PBS. This is within a similar trend of  $\mu_{FE}$  evolution for m-MoS<sub>2</sub> FETs for PBS (or NBS) in the literature [44,45]. For quantitative visualization

and its easy understanding of the trend of evolution for DOSs, all the information on the extracted DOSs is summarized in Table 1 (W/O CYTOP) and Table 2 (W/CYTOP), respectively. In the present work, with an adoption of the values in Tables 1 and 2, the information of DOSs before (or after) bias stress for m-MoS<sub>2</sub> FETs with (or without) CYTOP encapsulation is displayed in Fig. 7 for a clear delivery of the trend of evolution of DOSs.

### C. TCAD simulation

To validate the physical meaning of the extracted subgap-DOSs from the perspective of device operation, a technology computer-aided design (TCAD) simulation was performed using Atlas 2-D of SILVACO [55-57]. TCAD simulation was performed by changing Si-based model parameters and electrical parameters because multilayer MoS<sub>2</sub> is typically known to have an indirect bandgap. Thus, transfer characteristics for m-MoS<sub>2</sub> FETs via TCAD simulation were obtained from experimentally extracted DOSs,  $g(E)$ , by using optical charge pumping C-V spectroscopy. As shown in Fig. 8, we simulated I-V data with structural parameters and material parameters. Additionally, we enhanced the accuracy of the simulation by comparing the electrical parameters of the measured I-V data with the electrical parameters of the simulated I-V data. Fig. 9 shows changes in electrical properties according to DOS parameters. As a result, it is confirmed through simulation that DOSs near the conduction band have a significant impact on electrical parameters. In particular, because the DOS parameter  $N_{\text{Mid}}$  and  $N_{\text{SD}}$  reduction can contribute to the increase in mobility and current level in transfer curves, we fitted the mobility by using these values, leading to extraction of field effect mobility. In addition, doping concentration ( $N_d$ ) reduction can contribute to a decrease in  $V_{\text{th}}$ . Thus,  $V_{\text{th}}$  was extracted by fitting these parameters. The extracted DOS values are specified in Tables 1 and 2, respectively, and  $N_d = 2.7 \times 10^{17}$  (or  $1.0 \times 10^{17}$ ) cm<sup>-3</sup> for MoS<sub>2</sub> W/O (or W/) CYTOP. In addition, the actual physical dimension of W/L (= 30/10 μm) was used for this simulation study. Fig. 10 shows that the simulated I-V characteristics are compared with the experimental data obtained from the electrical measurement of the I-V characteristics for all bias stresses and encapsulation conditions. The transfer characteristics were measured at a fixed drain-to-source voltage ( $V_{\text{DS}}$ ) of 0.1 V at room temperature. All results indicate that the transfer characteristics in the TCAD simulation are nicely matched with the measured transfer characteristics, substantiating that extracted subgap-DOSs information is physically meaningful.

### IV. CONCLUSION

For the future application of backplanes in flat panel displays, along with hybrid integration Si devices with 2-dimensional transition metal dichalcogenides, reliable device operation and its securing stable device configuration with optimization of 2D semiconductors and dielectrics are starting points for practical circuit-level applications. Thus, in this study,

reliable and quantitative estimation of the bias stress instability of m-MoS<sub>2</sub> FETs for the respective PBS and NBS were systematically performed. To secure reliable m-MoS<sub>2</sub> FETs, the devices were encapsulated with CYTOP, leading to decoupling with external effects associated with ambient gas (e.g., O<sub>2</sub> and H<sub>2</sub>O) in air. As one of the systematic methods for the extraction of subgap-DOSs, optical charge-pumping capacity-voltage spectroscopy was adopted, and hence, the extraction of DOSs and their evolution of DOSs for the respective PBS (or NBS) were investigated. With respect to the extracted DOSs at midgap and shallow trap levels, originating from  $V_S$  and  $V_{S2}$ , respectively, peak positions were shifted upward after PBS, leading to a state transition from  $V_S$  to  $V_S(-1)$  by electron trapping in the subgap states. Moreover, states of  $V_S(-1)$ , which have a larger negative charge than that of  $V_S(0)$ , transitioned toward  $V_S(0)$ , and  $H_{S2}(0)$  was shifted toward  $H_{S2}(+1)$ , owing to the attraction of holes during NBS. In addition, compared with that of  $N_{\text{Mid}}$  for the initial state, the  $N_{\text{Mid}}$  peak with the highest value was changed from 0.50 eV to 0.37 eV (or 0.78 eV) after PBS (or NBS). Likewise, the  $N_{\text{SD}}$  peak was changed from the initial value of 0.17 eV to 0.05 eV (or 0.21 eV) after PBS (or NBS), accordingly. Variations in electrical parameters after bias stress rationally match the trend observed from DOSs information. Last, TCAD simulation substantiates that the extracted subgap DOSs information according to PBS (or NBS) is physically meaningful, leading to self-manifestation of the validity of the extracted DOSs information in I-V characteristics. Herein, the platform, which was secured for evaluation on subgap-DOSs for m-MoS<sub>2</sub> FETs, is expected to hint at the quantitative information behind the mechanism, which is closely related to device instabilities but hard to analyze due to previously reported methods associated active area limitation and unresolved information on both charge carriers and transport for each bias condition, relying on one-sided evaluation for either I-V or C-V characterization, respectively.

### V. REFERENCES

- [1] M. Roy and Mahmoodi-Meimand, "Leakage current mechanisms and leakage reduction techniques in deep-submicrometer CMOS circuits," *Proc. IEEE*, vol. 91, no. 2, pp. 305-327, 2003.
- [2] Z. Abbas and M. Olivieri, "Impact of technology scaling on leakage power in nano-scale bulk CMOS digital standard cells," *Microelectronics J.*, vol. 45, no. 2, pp. 179-195, 2014.
- [3] Q. H. Wang, K. Kalantar-Zadeh, A. Kis, J. N. Coleman, and M. S. Strano, "Electronics and optoelectronics of two-dimensional transition metal dichalcogenides," *Nat. Nanotechnol.*, vol. 7, no. 11, pp. 699-712, 2012.
- [4] D. Jariwala, V. K. Sangwan, L. J. Lauhon, T. J. Marks, and M. C. Hersam, "Emerging device applications for semiconducting two-dimensional transition metal dichalcogenides," *ACS Nano*, vol. 8, no. 2, pp. 1102-1120, 2014.
- [5] X. Huang, Z. Zeng, and H. Zhang, "Metal dichalcogenide nanosheets: Preparation, properties and applications," *Chem. Soc. Rev.*, vol. 42, no. 5, pp. 1934-1946, 2013.
- [6] M. Chhowalla, H. S. Shin, G. Eda, L. J. Li, K. P. Loh, and H. Zhang, "The chemistry of two-dimensional layered transition metal

- dichalcogenide nanosheets,” *Nat. Chem.*, vol. 5, no. 4, pp. 263–275, 2013.
- [7] Y. Y. Illarionov, A. J. Molina-Mendoza, M. Waltl, T. Knobloch, M. M. Furchi, T. Mueller, and T. Grasser, “Reliability of next-generation field-effect transistors with transition metal dichalcogenides,” *IEEE Int. Reliab. Phys. Symp. Proc.*, vol. 2018-March, pp. 5A.51–5A.56, 2018.
- [8] W. H. Lee, H. H. Choi, D. H. Kim, and K. Cho, “25th anniversary article: Microstructure dependent bias stability of organic transistors,” *Adv. Mater.*, vol. 26, no. 11, pp. 1660–1680, 2014.
- [9] Y. P. Venkata Subbaiah, K. J. Saji, and A. Tiwari, “Atomically Thin MoS<sub>2</sub>: A Versatile Nongraphene 2D Material,” *Adv. Funct. Mater.*, vol. 26, no. 13, pp. 2046–2069, 2016.
- [10] B. Radisavljevic, A. Radenovic, J. Brivio, V. Giacometti, and A. Kis, “Single-layer MoS<sub>2</sub> transistors,” *Nat. Nanotechnol.*, vol. 6, no. 3, pp. 147–150, 2011.
- [11] D. Jariwala, V. K. Sangwan, D. J. Late, J. E. Johns, V. P. Dravid, T. J. Marks, L. J. Lauhon, and M. C. Hersam, “Band-like transport in high mobility unencapsulated single-layer MoS<sub>2</sub> transistors,” *Appl. Phys. Lett.*, vol. 102, no. 17, Art. no. 173107, 2013.
- [12] G. He *et al.*, “Conduction Mechanisms in CVD-Grown Monolayer MoS<sub>2</sub> Transistors: From Variable-Range Hopping to Velocity Saturation,” *Nano Lett.*, vol. 15, no. 8, pp. 5052–5058, 2015.
- [13] H. Wang, L. Yu, Y.-H. Lee, Y. Shi, A. Hsu, M. L. Chin, L.-J. Li, M. Dubey, J. Kong and T. Palacios, “Integrated circuits based on bilayer MoS<sub>2</sub> transistors,” *Nano Lett.*, vol. 12, no. 9, pp. 4674–4680, 2012.
- [14] M. Choi, Y. J. Park, B. K. Sharma, S. R. Bae, S. Y. Kim, and J. H. Ahn, “Flexible active-matrix organic light-emitting diode display enabled by MoS<sub>2</sub> thin-film transistor,” *Sci. Adv.*, vol. 4, no. 4, Art. no. eaas8721, 2018.
- [15] R. Kumar, P. K. Kulriya, M. Mishra, F. Singh, G. Gupta, and M. Kumar, “Highly selective and reversible NO<sub>2</sub> gas sensor using vertically aligned MoS<sub>2</sub> flake networks,” *Nanotechnology*, vol. 29, Art. no. 464001, 2018.
- [16] S. Zandi, P. Saxena, M. Razaghi, and N. E. Gorji, “Simulation of CZTSSe Thin-Film Solar Cells in COMSOL: Three-Dimensional Optical, Electrical, and Thermal Models,” *IEEE J. Photovoltaics*, vol. 10, no. 5, pp. 1503–1507, 2020.
- [17] Y. Chen, G. Gao, J. Zhao, H. Zhang, J. Yu, X. Yang, Q. Zhang, W. Zhang, S. Xu, J. Sun, Y. Meng, and Q. Sun, “Piezotronic Graphene Artificial Sensory Synapse,” *Adv. Funct. Mater.*, vol. 29, no. 41, Art. no. 1900959, 2019.
- [18] X. Yang, J. Han, J. Yu, Y. Chen, H. Zhang, M. Ding, C. Jia, J. Sun, Q. Sun, and Z. L. Wang, “Versatile Triboiontronic Transistor via Proton Conductor,” *ACS Nano*, vol. 14, no. 7, pp. 8668–8677, 2020.
- [19] X. Yang, J. Yu, J. Zhao, Y. Chen, G. Gao, Y. Wang, Q. Sun, and Z. L. Wang, “Mechanoplastic Tribotronic Floating-Gate Neuromorphic Transistor,” *Adv. Funct. Mater.*, vol. 30, no. 34, Art. no. 2002506, 2020.
- [20] A. Rai, H. C. P. Movva, A. Roy, D. Taneja, S. Chowdhury, and S. K. Banerjee, “Progress in contact, doping and mobility engineering of MoS<sub>2</sub>: An atomically thin 2D semiconductor,” *Crystals*, vol. 8, no. 8, Art. no. 316, 2018.
- [21] S. Das, H. Y. Chen, A. V. Penumatcha, and J. Appenzeller, “High performance multilayer MoS<sub>2</sub> transistors with scandium contacts,” *Nano Lett.*, vol. 13, no. 1, pp. 100–105, 2013.
- [22] K. K. H. Smithe, C. D. English, S. V. Suryavanshi, and E. Pop, “Intrinsic electrical transport and performance projections of synthetic monolayer MoS<sub>2</sub> devices,” *2D Mater.*, vol. 4, no. 1, Art. no. 011009, 2017.
- [23] S. M. Gali, A. Pershin, A. Lherbier, J. C. Charlier, and D. Beljonne, “Electronic and Transport Properties in Defective MoS<sub>2</sub>: Impact of Sulfur Vacancies,” *J. Phys. Chem. C*, vol. 124, no. 28, pp. 15076–15084, 2020.
- [24] H. Yuan, H. Shen, J. Li, J. Shao, D. Huang, Y. Chen, P. F. Wang, S. J. Ding, A. Chin, and M. Li, “PBTI Investigation of MoS<sub>2</sub> n-MOSFET With Al<sub>2</sub>O<sub>3</sub> Gate Dielectric,” vol. 38, no. 5, pp. 677–680, 2017.
- [25] Y. Y. Illarionov, G. Rzepa, M. Waltl, T. Knobloch, A. Grill, M. M. Furchi, T. Mueller, and T. Grasser, “The role of charge trapping in MoS<sub>2</sub>/SiO<sub>2</sub> and MoS<sub>2</sub>/hBN field-effect transistors,” *2D Mater.*, vol. 3, no. 3, Art. no. 035004, 2016.
- [26] Y. Y. Illarionov, T. Knobloch, M. Waltl, G. Rzepa, A. Pospischil, D. K. Polyushkin, M. M. Furchi, T. Mueller, and T. Grasser, “Energetic mapping of oxide traps in MoS<sub>2</sub> field-effect transistors,” *2D Mater.*, vol. 4, no. 2, Art. no. 025108, 2017.
- [27] Y. Y. Illarionov, K. K. H. Smithe, M. Waltl, T. Knobloch, E. Pop, and T. Grasser, “Improved Hysteresis and Reliability of MoS<sub>2</sub> Transistors with High-Quality CVD Growth and Al<sub>2</sub>O<sub>3</sub> Encapsulation,” *IEEE Electron Device Lett.*, vol. 38, no. 12, pp. 1763–1766, 2017.
- [28] S. Choi, S. G. Seo, H. R. Yu, S. Y. Kim, D. H. Kim, and S. H. Jin, “Hydrophobic Polymer Encapsulation Effects on Subgap Density of States in Multilayered Molybdenum Disulfide Field-Effect Transistors,” *Phys. Status Solidi - Rapid Res. Lett.*, vol. 14, Art. no. 1900492, 2019.
- [29] M. Takenaka, Y. Ozawa, J. Han, and S. Takagi, “Quantitative evaluation of energy distribution of interface trap density at MoS<sub>2</sub> MOS interfaces by the Terman method,” *Tech. Dig. - Int. Electron Devices Meet. IEDM*, pp. 5.8.1–5.8.4, 2017.
- [30] H. Bae, C. K. Kim, and Y. K. Choi, “Characterization of intrinsic subgap density-of-states in exfoliated MoS<sub>2</sub> FETs using a multi-frequency capacitance-conductance technique,” *AIP Adv.*, vol. 7, no. 7, Art. no. 075304, 2017.
- [31] Q. Xu, Y. Sun, P. Yang, and Y. Dan, “Density of defect states retrieved from the hysteretic gate transfer characteristics of monolayer MoS<sub>2</sub> field effect transistors,” *AIP Adv.*, vol. 9, no. 1, Art. no. 015230, 2019.
- [32] K. Cho, W. Park, J. Park, H. Jeong, J. Jang, T. Y. Kim, W. K. Hong, S. Hong, and T. Lee, “Electric stress-induced threshold voltage instability of multilayer MoS<sub>2</sub> field effect transistors,” *ACS Nano*, vol. 7, no. 9, pp. 7751–7758, 2013.
- [33] S. Yang, S. Park, S. Jang, H. Kim, and J. Y. Kwon, “Electrical stability of multilayer MoS<sub>2</sub> field-effect transistor under negative bias stress at various temperatures,” *Phys. Status Solidi - Rapid Res. Lett.*, vol. 8, no. 8, pp. 714–718, 2014.
- [34] H. Qiu, L. Pan, Z. Yao, J. Li, Y. Shi, and X. Wang, “Electrical characterization of back-gated bi-layer MoS<sub>2</sub> field-effect transistors and the effect of ambient on their performances,” *Appl. Phys. Lett.*, vol. 100, no. 12, Art. no. 123104, 2012.
- [35] W. Park, J. Park, J. Jang, H. Lee, H. Jeong, K. Cho, S. Hong, and T. Lee, “Oxygen environmental and passivation effects on molybdenum disulfide field effect transistors,” *Nanotechnology*, vol. 24, no. 9, Art. no. 095202, 2013.
- [36] H. J. Kwon, J. Jang, S. Kim, V. Subramanian, and C. P. Grigoropoulos, “Electrical characteristics of multilayer MoS<sub>2</sub> transistors at real operating temperatures with different ambient conditions,” *Appl. Phys. Lett.*, vol. 105, no. 15, Art. no. 152105, 2014.
- [37] J. Roh, I.-T. Cho, H. Shin, G. Woo Baek, B. Hee Hong, J.-H. Lee, S. Hun Jin, and C. Lee, “Fluorinated CYTOP passivation effects on the electrical reliability of multilayer MoS<sub>2</sub> field-effect transistors,” *Nanotechnology*, vol. 26, no. 45, Art. no. 455201, 2015.
- [38] K. Jeon, C. Kim, I. Song, J. Park, S. Kim, S. Kim, Y. Park, J. H. Park, S. Lee, D. M. Kim, and D. H. Kim, “Modeling of amorphous InGaZnO thin-film transistors based on the density of states extracted from the optical response of capacitance-voltage characteristics,” *Appl. Phys. Lett.*, vol. 93, no. 18, Art. no. 182102, 2008.
- [39] H. Bae, H. Choi, S. Jun, C. Jo, Y. H. Kim, J. S. Hwang, J. Ahn, S. Oh, J. U. Bae, S. J. Choi, D. H. Kim and D. M. Kim, “Single-Scan monochromatic photonic capacitance-voltage technique for extraction of subgap DOS over the bandgap in amorphous semiconductor TFTs,” *IEEE Electron Device Lett.*, vol. 34, no. 12, pp. 1524–1526, 2013.
- [40] Y. G. Mo, M. Kim, and H. D. Kim, “Amorphous-oxide TFT backplane for large-sized AMOLED TVs,” *J. Soc. Inf. Disp.*, vol. 19, pp. 16–20, 2011.
- [41] H. H. Hsieh, T. Kamiya, K. Nomura, H. Hosono, and C. C. Wu, “Modeling of amorphous InGaZnO<sub>4</sub> thin film transistors and their subgap density of states,” *Appl. Phys. Lett.*, vol. 92, no. 13, pp. 10–13, 2008.
- [42] E. Fortunato, P. Barquinha, and R. Martins, “Oxide semiconductor thin-film transistors: A review of recent advances,” *Adv. Mater.*, vol. 24, no. 22, pp. 2945–2986, 2012.
- [43] K. Nomura, H. Ohta, A. Takagi, T. Kamiya, M. Hirano, and H. Hosono, “Room-temperature fabrication of transparent flexible thin-film transistors using amorphous oxide semiconductors,” *Nature*, vol. 432, no. 7016, pp. 488–492, 2004.

- [44] S. G. Seo and S. H. Jin, "Bias Temperature Stress Instability of Multilayered MoS<sub>2</sub> Field-Effect Transistors With CYTOP Passivation," *IEEE Trans. Electron Devices*, vol. 66, no. 5, pp. 2208–2213, 2019.
- [45] S. G. Seo, J. Joeng, K. Kim, K. Kim, and S. H. Jin, "Bias Stress Instability in Multilayered MoS<sub>2</sub> Field-Effect Transistors Under Pulse-Mode Operation," *IEEE Trans. Electron Devices*, vol. 67, no. 4, pp. 1864–1872, 2020.
- [46] S. Kc, R. C. Longo, R. Addou, R. M. Wallace, and K. Cho, "Impact of intrinsic atomic defects on the electronic structure of MoS<sub>2</sub> monolayers," *Nanotechnology*, vol. 25, no. 37, Art. no.375703, 2014.
- [47] J. Yang, H. Kawai, C. P. Y. Wong, and K. E. J. Goh, "Electrical Doping Effect of Vacancies on Monolayer MoS<sub>2</sub>," *J. Phys. Chem. C*, vol. 123, no. 5, pp. 2933–2939, 2019.
- [48] B. Zhao, C. Shang, N. Qi, Z. Y. Chen, and Z. Q. Chen, "Stability of defects in monolayer MoS<sub>2</sub> and their interaction with O<sub>2</sub> molecule: A first-principles study," *Appl. Surf. Sci.*, vol. 412, pp. 385–393, 2017.
- [49] K. Choi, S. R. A. Raza, H. S. Lee, P. J. Jeon, A. Pezeshki, S.-W. Min, J. S. Kim, W. Yoon, S.-Y. Ju, K. Lee, and S. Im, "Trap density probing on top-gate MoS<sub>2</sub> nanosheet field-effect transistors by photo-excited charge collection spectroscopy," *Nanoscale*, vol. 7, no. 13, pp. 5617–5623, 2015.
- [50] S. G. Seo, J. H. Hong, J. H. Ryu, and S. H. Jin, "Low-Frequency Noise Characteristics in Multilayer MoTe<sub>2</sub> FETs with Hydrophobic Amorphous Fluoropolymers," *IEEE Electron Device Lett.*, vol. 40, no. 2, pp. 251–255, 2019.
- [51] S. C. Lu and J. P. Leburton, "Electronic structures of defects and magnetic impurities in MoS<sub>2</sub> monolayers," *Nanoscale Res. Lett.*, vol. 9, no. 1, Art. no. 676, 2014.
- [52] A. Singh and A. K. Singh, "Origin of n -type conductivity of monolayer MoS<sub>2</sub>," *Phys. Rev. B*, vol. 99, no. 12, Art. no. 121201, 2019.
- [53] H. P. Komsa and A. V. Krasheninnikov, "Native defects in bulk and monolayer MoS<sub>2</sub> from first principles," *Phys. Rev. B - Condens. Matter Mater. Phys.*, vol. 91, no. 12, Art. no. 125304, 2015.
- [54] S. H. Song, M. K. Joo, M. Neumann, H. Kim, and Y. H. Lee, "Probing defect dynamics in monolayer MoS<sub>2</sub> via noise nanospectroscopy," *Nat. Commun.*, vol. 8, no. 1, Art. no. 2121, 2017.
- [55] D. L. Tiwari and K. Sivasankaran, "Impact of carrier concentration and bandgap on the performance of double gate GNR-FET," *Superlattices Microstruct.*, vol. 130, pp. 38–49, 2019.
- [56] D. L. Tiwari and K. Sivasankaran, "Nitrogen-doped NDR behavior of double gate graphene field effect transistor," *Superlattices Microstruct.*, vol. 136, Art. no. 106308, 2019.
- [57] D. L. Tiwari and K. Sivasankaran, "NDR Behavior of a Phosphorous-Doped Double-Gate MoS<sub>2</sub> Armchair Nanoribbon Field Effect Transistor," *J. Electron. Mater.*, vol. 49, no. 1, pp. 551–558, 2020.



**GA WOW YANG** received the B.S. degree in electrical engineering from Kookmin University, Seoul, South Korea, in 2020, where she is currently pursuing the M.S. degree with the Department of Electrical Engineering.



**SEUNG GI SEO** received the B.S. and M.S. degrees in electronic engineering from Incheon National University, Incheon, South Korea, in 2018 and 2020.

He is currently pursuing the Ph.D. degree in electronic engineering from Incheon National University, Incheon, South Korea.



**SUNGJU CHOI** received the B.S. and M.S. degrees in electrical engineering from Kookmin University, Seoul, South Korea, in 2016, where he is currently pursuing the Ph.D. degree with the Department of Electrical Engineering.



**DAE HWAN KIM** received the B.S., M.S., and Ph.D. degrees in electrical engineering from Seoul National University, Seoul, Korea, in 1996, 1998, and 2002, respectively.

He is currently a Professor with the School of Electrical Engineering, Kookmin University, Seoul, Korea. His current research interests include nano CMOS, oxide and organic thin film transistors, biosensors, and neuromorphic devices.



**SUNG HUN JIN** received the M.S. and Ph. D degrees in electrical engineering from Seoul National University (SNU), Seoul, South Korea, in 2000 and 2006, respectively.

He is currently an Associate Professor at Department of Electronic Engineering in Incheon National University. His current research interests include low dimensional materials (1D, 2D) based devices and circuits for flexible electronics.